Article | Received 6 September 2026; Revised 5 November 2026; Accepted 11 November 2026; Published 20 November 2026
https://doi.org/10.55092/am20260014

Minor-axis distortion of the TIF footprint in flexible ball-end tool polishing for ultra-precision optical manufacturing

Pengli Lei[1,†], Zikang Huang[2,†], Jianping Wang[2], Bo Zhong[1], Qingtang Wu[3], Bo Guo[3], Liang Zhao[3] and Chenchun Shi[2,4,*]

[1] Laser Fusion Research Center, China Academy of Engineering Physics, Mianyang, China
[2] School of Mechanical Engineering and Intelligent Manufacturing, Ningbo University, Ningbo, China
[3] Laboratory of Ultra-precision Fabrication, The 55th Research Institute of China North Industries Group Corporation, Changchun, China
[4] Ningbo Key Laboratory of Micro-nano Motion and Intelligent Control, Ningbo University, Ningbo, China

† These authors contributed equally to this work.

* Correspondence author; E-mail: shichenchun@nbu.edu.cn.

Highlights

- Dynamic dissipative stress governs the minor-axis asymmetric material removal of the TIF footprint, which quasi-static contact models cannot describe.
- Two Preston coefficients k_1 and k_2 separately quantify the elastic and dissipative contributions to material removal, generalizing the classical Preston model.
- The two-coefficient framework is verified with bonnet and solid rubber ball-end tools on two workpiece materials over a wide range of process conditions.

Abstract: Flexible bonnet polishing is one of the key technologies for high-efficiency deterministic ultra-precision manufacturing of large-aperture optical components. Accurate prediction of the Tool Influence Function (TIF) is critical for ensuring surface form accuracy. Conventional material removal models are mostly developed based on the Hertzian static contact theory and assume a constant pressure distribution at the polishing interface, which fail to describe the asymmetric material removal feature along the minor axis of practical elliptical polishing footprints. To address this issue, this paper proposes a material removal model considering the dynamic dissipation effect at the contact interface. The total contact stress within the contact zone between the flexible ball-end tool (FBET) and workpiece is decomposed into elastic and dissipative stress components. Two Preston coefficients are introduced to characterize their respective contributions to material removal. Combined with kinematic theory, a shear-velocity model in the contact zone is established, and a removal-function model is finally developed to predict the 2D profiles of polishing footprints along both the major and minor axes. Spot-polishing experiments are carried out using a solid rubber ball-end tool and a bonnet tool to investigate the influences

Copyright©2026 by the authors. Published by ELSP. This work is licensed under Creative Commons Attribution 4.0 International License, which permits unrestricted use, distribution, and reproduction in any medium provided the original work is properly cited.

of key process parameters on material removal depth (MRD) and footprint morphology. The results demonstrate that the proposed model can accurately predict the 2D profiles of polishing footprints along both major and minor axes under different tool types and process conditions. In particular, it can quantitatively characterize the pressure distribution shift and asymmetric material removal distortion induced by dynamic tool entry and exit along the minor axis. The predicted results show good consistency with experimental data in both trend and magnitude. This study reveals the formation mechanism of asymmetric distortion along the minor axis in FBET polishing and provides a theoretical foundation for the optimization and control of high-efficiency deterministic optical polishing processes.

Keywords: bonnet polishing; flexible ball-end tool; material removal; tool influence function; minor-axis distortion; dynamic contact

1. Introduction

1.1. Background review

High-efficiency ultra-precision manufacturing technologies for advanced optics have become a core pillar of the nation's high-end manufacturing sector. Driven by the ongoing progress in key fields including laser-driven inertial confinement fusion, space-based Earth observation, deep-space exploration, and extreme ultraviolet (EUV) lithography, the demand for large-aperture optical components with high surface form accuracy and superior surface quality keeps growing. Both China's Shenguang facility and the U.S. National Ignition Facility (NIF) represent some of the largest and most complex optical systems built to date, whose internal functional units require tens of thousands of optical components [1,2]. Another typical example is the James Webb Space Telescope (JWST). To achieve high-quality imaging, it demands nanometer-level surface form accuracy across its meter-scale aperture [3]. The question of how to realize rapid batch fabrication of optical components while ensuring machining quality and precision, and substantially boosting production efficiency, has thus emerged as a challenge of considerable significance [4].

To meet the requirements of high-precision and high-efficiency manufacturing of large-aperture optical elements, various ultra-precision machining technologies have been developed, including magnetorheological finishing (MRF) [5], fluid jet polishing (FJP) [6], small elastic tool polishing (SETP) [7], shear-thickening polishing (STP) [8], ultrasonic vibration chemical-mechanical polishing (UV-CMP) [9,10], and ion beam figuring (IBF) [11]. By contrast, flexible bonnet polishing features excellent conformability to curved surfaces, high removal efficiency, and controllable accuracy. It can be used both for uniform polishing with efficient material removal and for corrective polishing aimed at surface form convergence. As a deterministic finishing method with great potential for optical curved surfaces [12], it has become an important step in the ultra-precision manufacturing process chain for large-aperture optical components. In bonnet polishing, the tool influence function (TIF) can be modeled, and the polishing footprint size can be adjusted by the process parameters [13]. In deterministic polishing, surface generation is mainly attributed to the two-dimensional convolution between the TIF and the dwell time map along a prescribed polishing path [14]. Therefore, establishing a stable and predictable material removal model that can accurately reproduce the actual TIF footprint is key to improving surface figure prediction accuracy and process controllability.

In fact, considerable progress has been achieved in theoretical modeling and experimental investigations on the material removal characteristics of bonnet polishing. Depending on the scale of interest, existing studies can be categorized into macro-scaled TIF models and micro-scaled material removal models. Macro-models are generally built upon the Preston equation, where material removal is expressed as the product of the contact-zone pressure, the contact-zone shear velocity, dwell time, and the Preston coefficient. Among these, shear velocity modeling based on kinematic theory is relatively well-established and has reached broad consensus within the research community. Nevertheless, diverse approaches still exist for modeling the pressure distribution within the contact zone, which mainly fall into two categories: analytical modeling based on the Hertzian static contact theory and numerical modeling via FEA [15–17]. In contrast, micro-models focus more on the three-body interactions among abrasive grains, polishing pad and workpiece. Deng *et al.* [18] combined the Hertzian contact theory with abrasive scratching theory to construct a micro-scaled material removal volume model and validated it experimentally. Shi *et al.* [19] investigated the micro-contact behaviors among polishing slurry, polishing pad and workpiece, and established a micro-scaled material removal model based on tribological theory to interpret the nonlinear material removal mechanism. Most of the aforementioned researches adopt a static assumption for the polishing interfacial pressure, treating the pressure distribution predicted by Hertzian contact theory or FEA as nearly constant during polishing. However, in practical polishing with FBETs, the tool operates under complex working conditions involving dynamic rotation and fluid slurry [20]. The pressure distribution over the contact zone dynamically varies under the influences of tool motion, hydrodynamic pressure effect and other factors. Accordingly, directly adopting static contact pressure models for material removal modeling is highly likely to introduce considerable prediction errors, yielding discrepancies between the theoretically calculated TIF shape and the actual polishing footprint.

Nonetheless, a small number of existing studies have taken the dynamic effects of interfacial contact pressure into consideration. Although Shi *et al.* [21] reported dynamic contact pressure during FBET polishing and revealed the asymmetric distortion feature of the 2D profile along the minor axis of the footprint, their work remains largely qualitative and lacks mathematical formulations for quantitative calculation. Cao *et al.* [22,23] proposed a microscopic material removal model incorporating dynamic effects, whereas their analyses mainly emphasized the material removal mechanism along the major axis of the elliptical polishing footprint, thereby lacking systematic interpretation of the removal mechanism along the minor axis (*i.e.*, the tool entry-exit direction). Since the overall surface topography generated in polishing can be regarded as the two-dimensional convolution of the TIF and the dwell-time distribution [14], prediction errors along either the major or minor axis will distort the material removal distribution. Therefore, establishing a theoretical model capable of simultaneously characterizing the removal behaviors along both the major and minor axes of the TIF footprint constitutes a critical yet unresolved challenge, which forms one of the key research objectives of this paper.

1.2. Scientific problem and research objectives

Inspired by relevant previous studies [23,24], the generic scientific finding of this work is that the minor-axis asymmetric material removal in FBET polishing originates from the dynamic characteristics of the contact pressure at the tool-workpiece interface. The interfacial contact pressure is decomposed into elastic and dissipative components, and two Preston coefficients, k_1 and k_2, are introduced to quantify their

individual contributions to material removal, thereby establishing a material removal model. Polishing experiments employing two representative FBETs (a bonnet tool and a solid elastic ball-end tool) are performed to validate the correctness and reliability of the proposed model and uncover the asymmetric material removal mechanism along the minor axis of the polishing footprint. This investigation enriches and advances the theoretical framework for high-efficiency deterministic polishing and offers valuable insights for the mass production of high-performance optical components.

2. Theoretical modeling

In optical sub-aperture polishing, the Preston theory is widely adopted for the modeling of material removal. To reveal the material removal mechanism underlying minor axis distortion of the elliptical polishing footprint in FBET polishing and clarify the nature of asymmetric material removal along the minor axis direction, this paper constructs a corresponding material removal prediction model based on the Preston equation, as shown in Equation (1). The material removal depth (MRD) is jointly determined by the interfacial contact pressure P, contact-zone shear velocity V, dwell time t_d, and the Preston coefficient k.

$$MRD = kPVt_d \tag{1}$$

Herein, the Preston coefficient k is determined via spot polishing experiments, and t_d serves as a known input parameter. The key parameters P and V are modeled separately in the following sections.

2.1. Dynamic contact pressure P

Both the bonnet tool and the solid rubber ball-end tool are elastomers, and their plasticity index is only about one-tenth that of metals. Therefore, their contact behavior is predominantly elastic. Researchers often apply Hertz contact theory to model the pressure distribution in the contact zone of FBET polishing [25]. However, Hertz contact theory is intended for static contact between perfectly elastic bodies under dry conditions. In actual polishing, the contact between the FBET and the workpiece is dynamic and lubricated by polishing slurry, and the FEBT itself is not a perfectly elastic body. As illustrated in Figure 1, the two-dimensional profile of the actual elliptical polishing footprint along the minor axis is not symmetric but exhibits obvious asymmetric characteristics. Therefore, the conventional Preston model based on static Hertz contact has limitations in describing flexible bonnet or solid rubber ball-end tool polishing, and the contact pressure model requires prior revision.

According to the research conducted by Brilliantov, Pöschel and co-workers [24–26], the total contact stress P can be treated as a linear superposition of the elastic component σ_{zz}^{el} and the dissipative component σ_{zz}^{dis}, as shown in Figure 2. First, the elastic stress component σ_{zz}^{el} is solved. It corresponds to the known solution of the Hertz contact problem and can be expressed as [23]

$$\sigma_{zz}^{el} = E_1 \frac{\partial u_z}{\partial z} + \left(E_2 - \frac{E_1}{3} \right) \left(\frac{\partial u_x}{\partial x} + \frac{\partial u_y}{\partial y} + \frac{\partial u_z}{\partial z} \right) = P_0 \left(1 - \frac{x^2}{a^2} - \frac{y^2}{b^2} \right)^{1/2} \tag{2}$$

where u_x, u_y and u_z denote the displacement fields in the x, y, and z directions for the classical Hertz contact problem. $E_1 = Y/(1+v)$ and $E_2 = Y/3(1-2v)$ are defined as the elastic material constants. Herein, Y and v stand for the Young's modulus and Poisson's ratio of the polishing pad, respectively. According to references [21,27], a denotes the semi-minor axis of the elliptical contact region, b signifies the

semi-major axis, and P_0 is the maximum contact pressure. Their mathematical expressions are clearly given by Equations (3), (4), and (5), respectively.

$$P_0 = \left(\frac{6F_{\text{eff}} \cdot (E^*)^2}{\pi^3 R_{\text{t}}^2} \right)^{\frac{1}{3}} \tag{3}$$

$$a = \left(\frac{3\theta^2 \beta F_{\text{eff}} R}{\pi E^*} \right)^{\frac{1}{3}} \tag{4}$$

$$b = \frac{\sqrt{h(h-2R_{\text{w}})(h-2R_{\text{t}})(2R_{\text{w}}-h+2R_{\text{t}})}}{(2R_{\text{w}}-h+2R_{\text{t}})} \tag{5}$$

where R_{t} and R_{w} represent the radius of the FBET and the curvature radius of the workpiece, respectively. h is the tool offset, θ means the ratio between the major-axis and minor-axis lengths of the ellipse (see Equation (6)). β is a parameter associated with the elliptical contact zone (see Equation (7)). Besides, $R = 1/(A + B)$. E^* denotes the equivalent elastic modulus (see Equation (9)).

$$\theta = 1.0339 \left(\frac{B}{A} \right)^{0.636} \tag{6}$$

$$\beta = 1.0003 + 0.5968 \left(\frac{A}{B} \right) \tag{7}$$

$$A = B = \frac{1}{R_{\text{t}}} \tag{8}$$

$$E^* = \left(\frac{1-v_1^2}{E_3} + \frac{1-v_2^2}{E_4} \right)^{-1} \tag{9}$$

Here, E_3, v_1 and E_4, v_2 correspond to the Young's modulus and Poisson's ratio of the FBET and workpiece materials, respectively [28]. The effective contact force F_{eff} can be approximately regarded as the vector sum of the normal load F_{n} and the tangential load F_τ [27], as formulated in Equations (10)–(12), where parameter α denotes the precession angle.

$$F_{\text{n}} = \frac{4}{3} E^* R_{\text{t}}^{\frac{1}{2}} (h)^{\frac{3}{2}} \tag{10}$$

$$F_\tau = F_{\text{n}} \tan\alpha \tag{11}$$

$$F_{\text{eff}} = \sqrt{F_{\text{n}}^2 + F_\tau^2} = F_{\text{n}} \sqrt{1 + \tan^2\alpha} \tag{12}$$

Subsequently, the dissipative stress component σ_{zz}^{dis} is determined. Based on kinematic theory and contact mechanics [22,29], σ_{zz}^{dis} can be written as

$$\begin{aligned} \sigma_{zz}^{dis} &= \eta_1 \frac{\partial \dot{u}_z}{\partial z} + \left(\eta_2 - \frac{\eta_1}{3} \right) \left(\frac{\partial \dot{u}_x}{\partial x} + \frac{\partial \dot{u}_y}{\partial y} + \frac{\partial \dot{u}_z}{\partial z} \right) = -\frac{(1-2v)(1+v)}{Y} \\ &* \frac{\omega \cos\alpha \left(2\eta_2 + \eta_1/3\right) P_0 x (h - R_{\text{t}})}{a^2} * \left(1 - \frac{x^2}{a^2} - \frac{y^2}{b^2} \right)^{-1/2} + \frac{(1-v)^2}{Y} * \frac{\omega \cos\alpha \left(2\eta_2 + \eta_1/3\right) \pi P_0 x}{2a} \end{aligned} \tag{13}$$

where $\dot{u}_x$, $\dot{u}_y$, $\dot{u}_z$ represent the time derivatives of the displacement-field components along the x, y, and z directions, respectively. ω denotes the angular velocity. η_1 is the shear viscosity coefficient, which characterizes the viscous dissipation caused by the shear deformation of the polishing pad during dynamic contact. η_2 is the volumetric viscosity coefficient, which characterizes the volumetric viscous dissipation caused by the compression and relaxation of the pad material during the dynamic indentation and rebound of the tool. At this point, both σ_{zz}^{el} and σ_{zz}^{dis} are obtained.

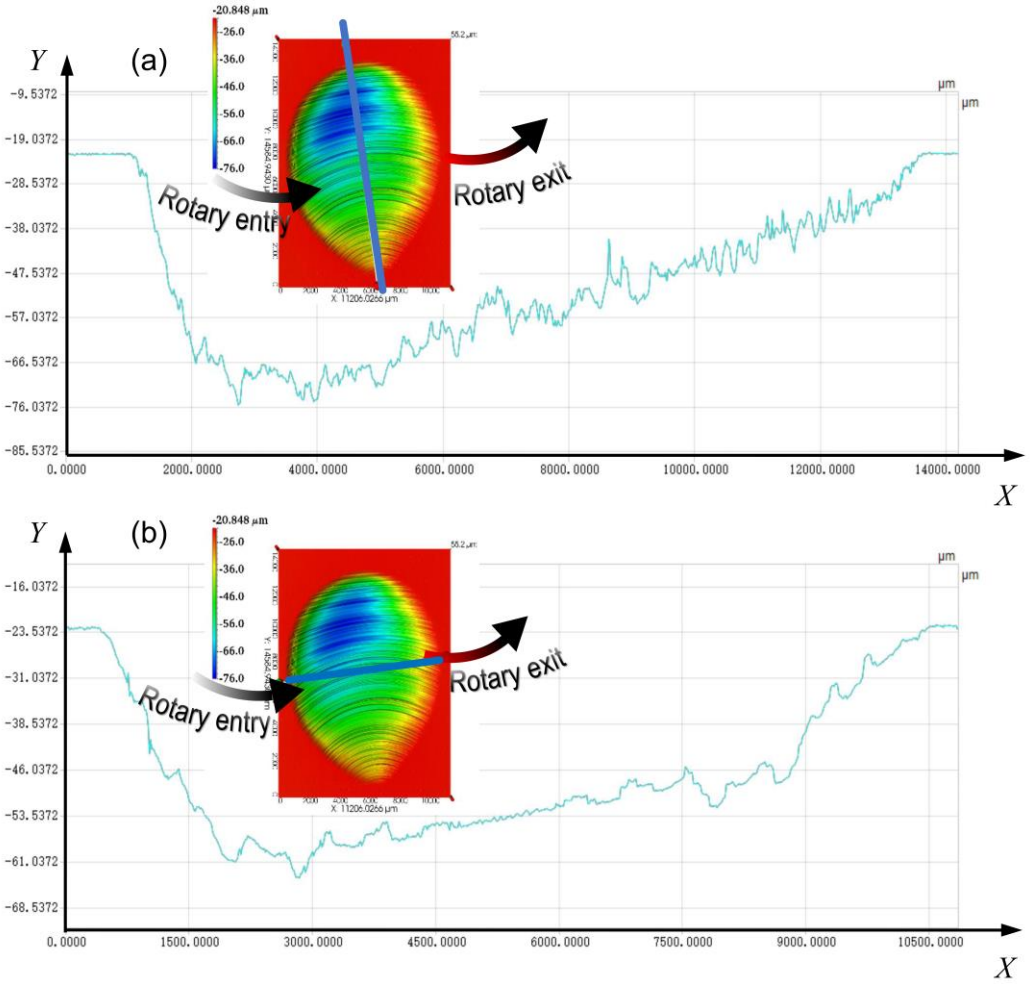


Figure 1. Polishing footprint morphology and corresponding 2D profiles obtained by elastic rubber ball-end tool polishing at experimental parameters of n = 1000 rpm, h = 1.2 mm, α = 23 deg. **(a)** Major axis; **(b)** Minor axis.

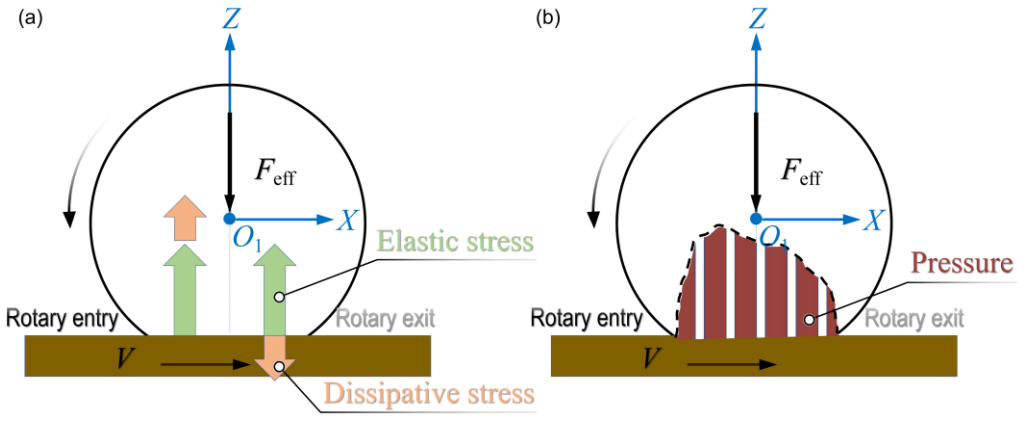


Figure 2. Schematic diagram of contact-pressure distribution for the FBET.

2.2. Contact-zone shear velocity V

Taking the bonnet polishing as the example, it adopts a unique precessional motion mode, where the tool rotation axis forms a certain angle α with the local normal of the workpiece surface. Based on kinematic theory, the shear velocity exerted by the bonnet tool on the workpiece surface within the polishing contact zone can be derived. As shown in Figure 3, the flexible bonnet tool with radius R_t compresses the workpiece downward with an indentation depth h (*i.e.*, tool offset h), generating an elliptical contact zone centered at O_2. Point F denotes an arbitrary point located within this contact zone. A Cartesian coordinate system $O_2X_2Y_2Z_2$ is established with O_2, the centre of the contact zone, as the origin. Under this coordinate system, point F can be expressed as $(x, y, 0)$. The rotation of axis L provides the driving source for the shear velocity V. Accordingly, the calculation of V should be performed within the O_1XYZ coordinate system. The coordinates of point F in the O_1XYZ frame can be readily obtained as

$$\boldsymbol{O_1F} = \boldsymbol{O_1O_2} + \boldsymbol{O_2F} = \begin{pmatrix} 0 & 0 & -(R_t - h) \end{pmatrix} + \begin{pmatrix} x & y & 0 \end{pmatrix} = \begin{pmatrix} x & y & -(R_t - h) \end{pmatrix} \tag{14}$$

The angular velocity of axis L can be expressed in vector form as

$$\boldsymbol{\omega} = \frac{2\pi n}{60}\begin{pmatrix} 0 & -\sin\alpha & \cos\alpha \end{pmatrix} \tag{15}$$

Combining Equation (14) and (15), the relative velocity of point F within the polishing contact zone in the O_1XYZ coordinate system is written as

$$\begin{aligned} v_F = \boldsymbol{\omega} \times \boldsymbol{O_1F} &= \begin{vmatrix} \boldsymbol{i} & \boldsymbol{j} & \boldsymbol{k} \\ 0 & \frac{2\pi n}{60}(-\sin\alpha) & \frac{2\pi n}{60}\cos\alpha \\ x & y & (-R_t + h) \end{vmatrix} \\ &= \frac{2\pi n}{60}\left[(-\sin\alpha)(-R_t + h) - y\cos\alpha\right]\boldsymbol{i} + \left(\frac{2\pi n}{60}x\cos\alpha\right)\boldsymbol{j} + \left(\frac{2\pi n}{60}x\sin\alpha\right)\boldsymbol{k} \end{aligned} \tag{16}$$

Material shear removal within the contact zone is associated with velocity components along the X and Y axes and independent of the Z-direction component. Hence, the shear velocity V can be further formulated as

$$V = \sqrt{v_{Fx}^{\ 2} + v_{Fy}^{\ 2}} = \frac{2\pi n}{60}\sqrt{\left(y\cos\alpha + (h - R_t)\sin\alpha\right)^2 + (x\cos\alpha)^2} \tag{17}$$

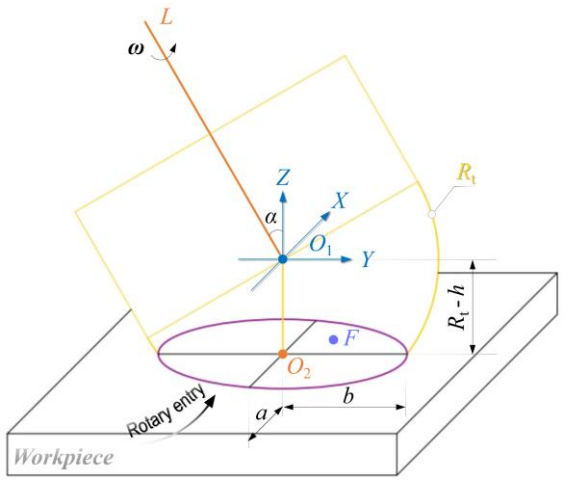


Figure 3. Schematic for shear velocity modelling.

2.3. Determination of material removal model

Based on Equation (2) and Equation (13), Equation (1) can be rewritten as

$$MRD = k\left(\sigma_{zz}^{el} + \sigma_{zz}^{dis}\right)\cdot V \cdot t_{\mathrm{d}} \tag{18}$$

Predictive investigations on the 2D profile along the major axis direction of the polishing footprint are relatively mature and widely reported [30]. For the 2D profile along the major axis direction, $x = 0$ holds, and accordingly Equation (13) yields zero. Hence, Equation (18) can be further simplified for predicting the 2D profile along the major axis of the polishing footprint as

$$MRD = k\sigma_{zz}^{el} V t_{\mathrm{d}} \tag{19}$$

As can be observed from Figures 2 and 3, unlike the minor axis direction, the major axis direction of the polishing footprint undergoes no dynamic entry-exit motion of the FBET and corresponds to quasi-static contact. Consequently, the contact pressure in Equation (19) is purely the static Hertz contact pressure given by Equation (2). By contrast, dynamic entry-exit behaviour of the FBET exists along the minor axis direction of the polishing footprint, hence, Equation (18) should be adopted to analyse the material removal behaviour. In the work reported by Cao *et al.* [22,23], Equation (18) was directly employed to analyse material removal in bonnet polishing. Nevertheless, their research focused on the profile characteristics of the polishing footprint along the major axis direction and did not carry out systematic and thorough investigations on the profile evolution along the minor axis direction. Theoretically, Equation (18) implies a 1:1 weight ratio between σ_{zz}^{el} and σ_{zz}^{dis}. However, practical FBET polishing involves complex factors such as polishing slurry, abrasive particles, and workpiece material properties. Furthermore, the FBET is composed of a polyurethane polishing pad bonded to a ball-end substrate. Owing to these practical complex factors, the weight ratio between the two stress components may deviate from 1:1. To separately characterize their respective contributions to material removal, two Preston coefficients k_1 and k_2 are introduced in this work, and the revised prediction model for *MRD* is finally established as follows:

$$MRD = k_1\sigma_{zz}^{el} V t_{\mathrm{d}} + k_2\sigma_{zz}^{dis} V t_{\mathrm{d}} \tag{20}$$

It can be seen that Equation (20) is capable of predicting not only the 2D profile along the major axis of the polishing footprint (*i.e.*, Equation (19)) but also that along the minor axis. When $k_2 = 0$, the dissipative term vanishes and the model degenerates into $MRD = k_1\sigma_{zz}^{el} V t_{\mathrm{d}}$, in which material removal is determined solely by the elastic stress component. Letting $k_1 = k$ and $\sigma_{zz}^{el} = P$, the classical Preston equation $MRD = kPVt_{\mathrm{d}}$ is recovered. The classical Preston model can therefore be regarded as a special case of the model proposed in this work in which the dynamic dissipative contribution is neglected. In this sense, the proposed model extends the classical Preston model rather than replacing it.

From a purely mathematical point of view, it is feasible to merge the elastic and the dissipative stress into a single equivalent stress and to describe the material removal with a single Preston coefficient. The main purpose of introducing two Preston coefficients in this work is, however, not to construct a mathematically unique expression for material removal, but to preserve the interpretability of the contributions of the different stress components. The elastic stress is determined by the static contact and is independent of the rotational speed, whereas the dissipative stress depends on the

rotational speed. If a single Preston coefficient were used, the same mathematical description could be obtained, but the independent contributions of the elastic and the dissipative stress to material removal would be merged. The two-coefficient form therefore reflects the physical process more directly and also makes it possible to reproduce the speed-dependent evolution of the removal asymmetry with a fixed pair of coefficients.

3. Results and discussion

3.1. Evaluation of k_1 and k_2

Before solving the material removal model expressed in Equation (20), the Preston coefficients k_1 and k_2 must be determined by spot polishing experiments. Existing studies mostly analyse the 2D profile along the major axis direction of the polishing footprint [31–34]. According to Equation (1) and (19), Equation (21) can be applied to directly determine the coefficient k. Specifically, at least three points are randomly selected from the 2D cross-section profile along the major axis of the polishing footprint, and their measured depth values are denoted as MRD_{d1}, MRD_{d2}, MRD_{d3}. The denominator term in Equation (21) is calculated theoretically, followed by the computation of k_{d1}, k_{d2}, k_{d3}. The final value of k is available by averaging these three calculated values. This approach for determining the Preston coefficient k has been widely accepted by peer researchers.

Nevertheless, since two coefficients k are introduced in Equation (20), modifications to the above-mentioned conventional method are required. Analysis of the dissipative stress tensor given in Equation (13) reveals that the contribution of the dissipative stress component to total contact stress can be neglected along the major axis direction of the elliptical polishing footprint (*i.e.*, the characteristic cross-section at $x = 0$). Accordingly, the 2D material removal profile along the major axis mainly reflects the contribution from the elastic stress component σ_{zz}^{el}. Based on this feature, as shown in Equation (22), k_2 exerts no influence on the calculation when solving for k_1. Hence, $k_1 = 3.37288 \times 10^{-13}$ can be computed using the data presented in Figure 4 and the experimentally measured removal depth along the major axis. With k_1 already determined, k_2 is further identified from the measured 2D profile along the minor axis direction of the polishing footprint. Using Equation (23), the data in Figure 4 and the measured removal depth along the minor axis, $k_2 = 7.11282 \times 10^{-12}$ is obtained.

$$k = \frac{MRD_{\text{exp}}}{PVt_{\text{d}}} \tag{21}$$

$$k_1 = \frac{MRD_{\text{exp}} - k_2\sigma_{zz}^{dis}Vt_{\text{d}}}{\sigma_{zz}^{el}Vt_{\text{d}}} = \frac{MRD_{\text{exp}}}{\sigma_{zz}^{el}Vt_{\text{d}}} \tag{22}$$

$$k_2 = \frac{MRD_{\text{exp}} - k_1\sigma_{zz}^{el}Vt_{\text{d}}}{\sigma_{zz}^{dis}Vt_{\text{d}}} \tag{23}$$

where MRD_{exp} represents the actual material removal depth at an arbitrary point $F(x, y)$ within the contact zone (shown in Figure 3) after the polishing dwell time t_{d}. Figure 4 presents the polishing footprint data acquired from spot polishing experiments.

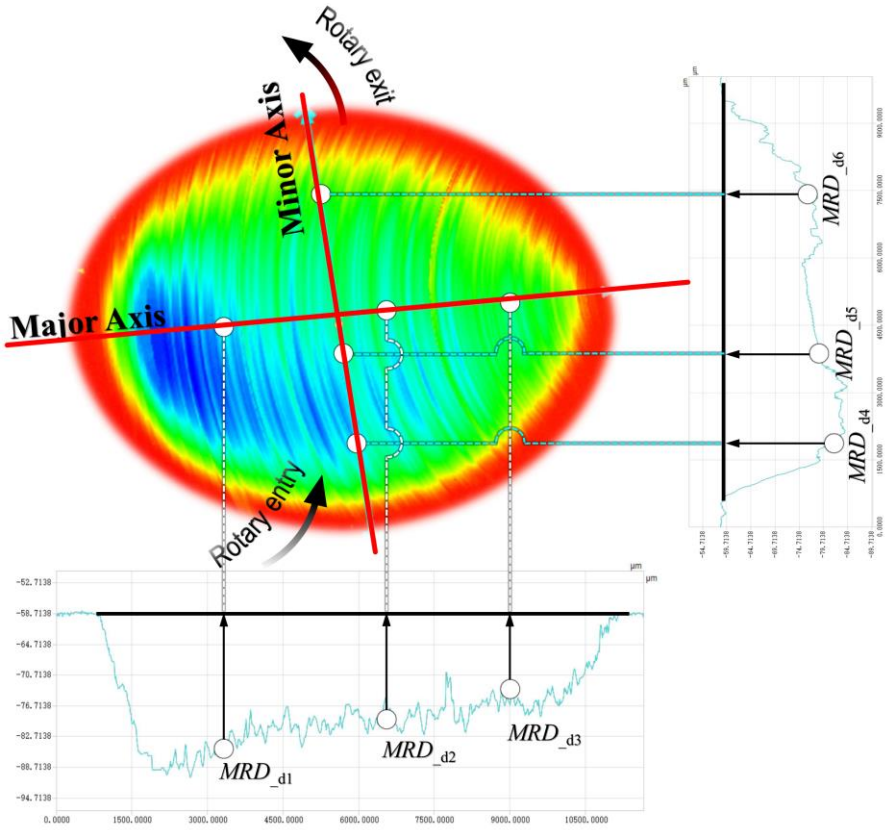


Figure 4. Two-dimensional profiles along the major axis and minor axis of the polishing footprint measured under experimental conditions of n = 1000 rpm, h = 0.8 mm, α = 23 deg, t_d = 2 min.

The coefficients k_1 and k_2 are not intrinsic material constants that are completely independent of the machining conditions, but Preston coefficients obtained by experimental calibration for a given tool, workpiece material, abrasive system and set of machining parameters. They inevitably contain the combined influence of the complex interfacial interactions [35,36]. They are, however, not merely mathematical fitting parameters, since they have a clear physical distinction: k_1 is determined solely from the major-axis profile, along which the dissipative stress is theoretically zero, so it independently characterizes the material removal caused by the elastic stress. k_2 is then determined from the minor-axis profile after k_1 has been fixed, so it independently characterizes the additional material removal caused by the dissipative stress. Although both coefficients originate from experimental calibration, they correspond to different stress sources and are identified from experimental information along different spatial directions. They therefore have independent physical bases.

In addition, these Preston coefficients do not remain unchanged as the tool wears. Tool wear or a change in the pad condition alters the contact stiffness, the real contact area, the local friction, the action of the abrasive grains and the slurry supply, all of which affect the material removal depth and hence the Preston coefficients. These coefficients are therefore not recalculated as a matter of routine, but they must be re-examined when the wear or the change in the pad condition is large enough to shift the predicted TIF depth and width or the degree of minor-axis asymmetry beyond the acceptable range of the calibrated model. In that case the original calibration should be reviewed and, if necessary, repeated. Conversely, as long as the tool condition and the process window remain stable and the validation experiments show that the prediction accuracy remains acceptable, a single set of calibrated coefficients can be applied across experiments without recalibration.

3.2. Experimental validation with solid rubber ball-end tool polishing

The two typical tools employed in FBET polishing are the solid rubber ball-end tool and the bonnet tool. Both belong to sub-aperture polishing tools. Parameters such as rotational speed, tool offset and precession angle can be adjusted to control the contact area and pressure distribution between the tool and workpiece. To verify the effectiveness of the established model as well as its adaptability for different FBETs, spot polishing experiments are carried out using these two types of FBETs, respectively.

For spot polishing experiments with the solid rubber ball-end tool, single-factor experiments concerning the precession angle, spindle rotational speed and tool offset are performed. In each group of experiments, only one process parameter is varied while the others remain unchanged. The predicted 2D profiles along the major axis and minor axis obtained from the proposed material removal model are compared against the experimentally measured polishing footprint profiles. In this manner, the influences of each parameter on the MRD and asymmetric distortion of the polishing footprint can be analyzed, and the reliability of the developed material removal model under different working conditions can be validated. Polishing experiments are conducted on a Jingdiao JDEGR150 five-axis CNC machining centre, as illustrated in Figure 5. The polishing specimen is S136 steel with a Young's modulus of 206 GPa and a Poisson's ratio of 0.3. Prior to polishing, all S136 steel specimens are uniformly ground using 1000-grit sandpaper to achieve consistent surface roughness. The polishing slurry is prepared by mixing 4 μm-sized alumina powder with deionised water at a mass concentration of 5%, without additional chemical additives. A SuperView W13D surface profiler is utilized to characterise the morphology of the polishing footprint.

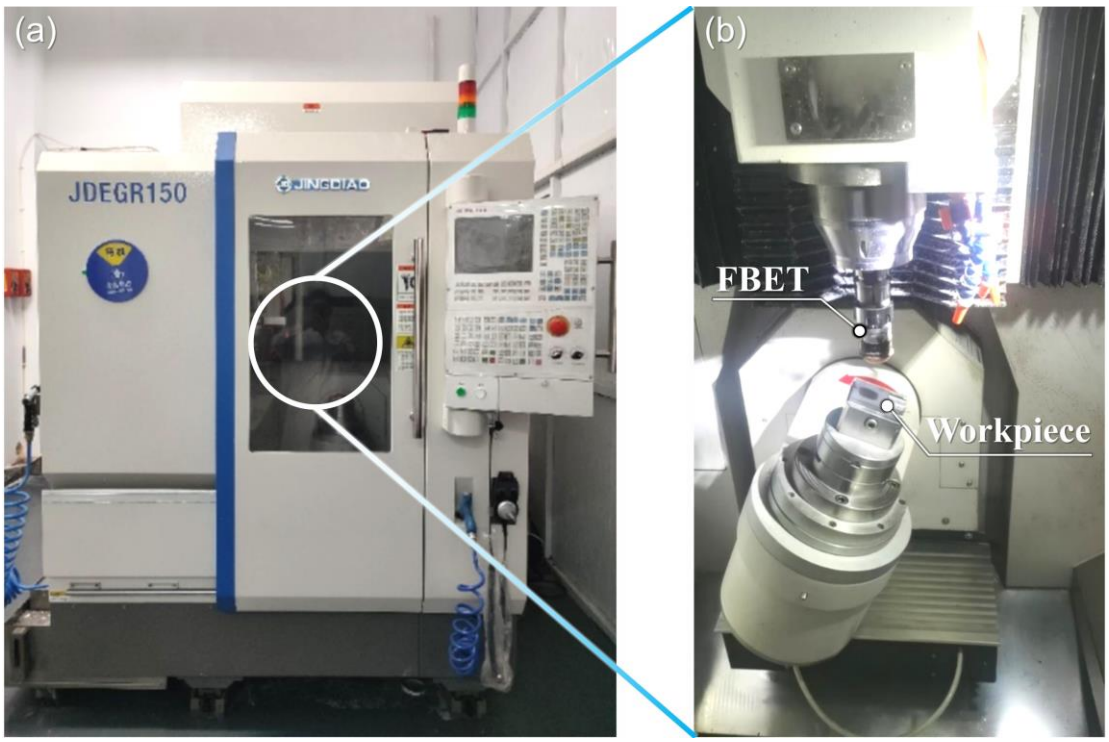


Figure 5. Five-axis CNC machining centre. **(a)** Overall view of the machine tool; **(b)** Internal structure.

3.2.1. Precession angle

Experimental investigations on the precession angle α are first carried out. Detailed experimental parameters are summarized in Table 1, and the corresponding predicted and measured results of the polishing footprint are presented in Figure 6. In general, the predicted results are in reasonable agreement with the variation trend of measured polishing footprint data, demonstrating the credibility of the established material removal model. As shown in Figure 6, the theoretically predicted MRDs along both the major axis and minor axis increase with rising precession angle. Nevertheless, the experimentally measured MRD along the major axis hardly increases when α increases from 23 degree to 25 degree. A larger precession angle may shorten the ploughing trajectory length of abrasive grains on the workpiece surface, reduce the number of effective participating abrasives, and impair the stable supply of polishing slurry in local regions. Consequently, the actual MRD no longer increases further. Hence, a larger precession angle does not always yield better performance. The precession angle should be set to guarantee sufficient shearing action while avoiding excessive tool tilt.

Table 1. Single-factor experimental parameters for precession angle (solid rubber ball-end tool).

h **(mm)**	***n*** **(rpm)**	***α*** **(deg)**
0.6	1000	21
		23
		25

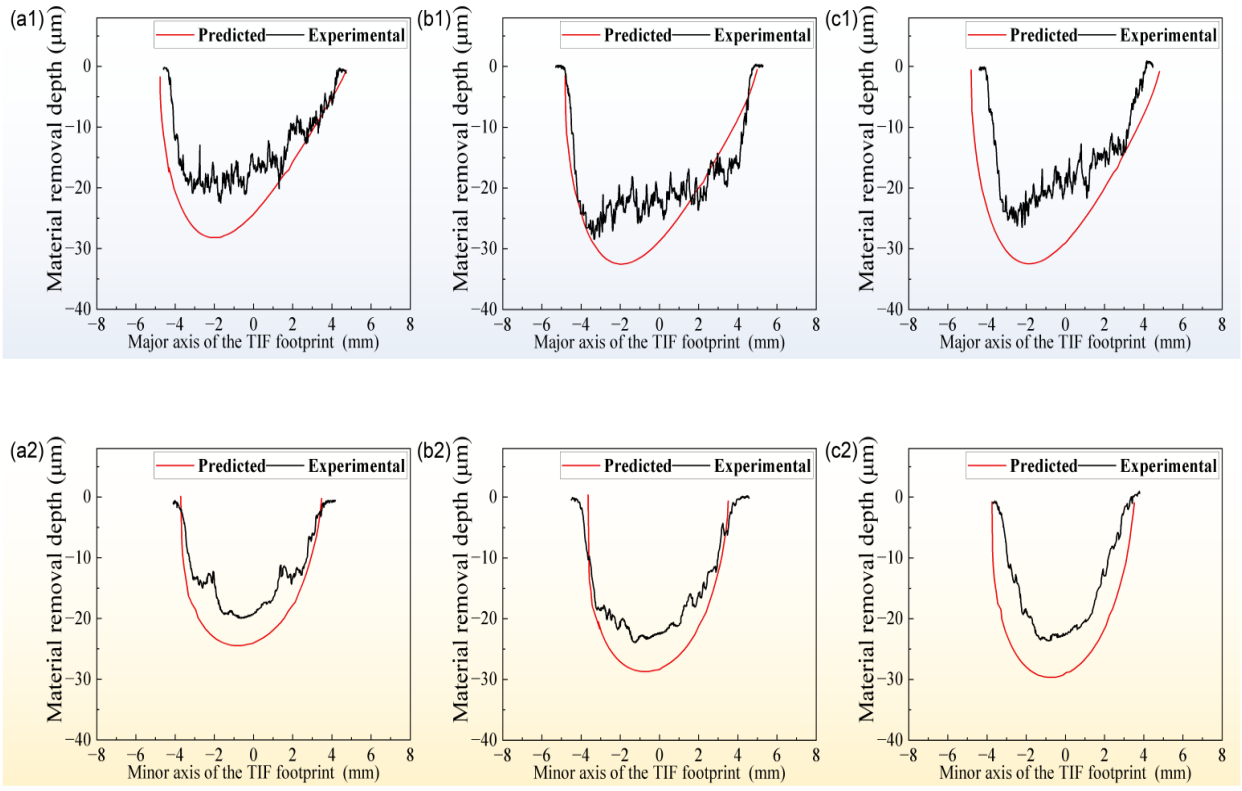


Figure 6. Comparison between predicted and measured polishing footprint results for different precession angles. **(a)** α = 21 deg; **(b)** α = 23 deg; **(c)** α = 25 deg.

3.2.2. Rotational speed

Afterwards, experiments regarding rotational speed n are implemented. Detailed experimental parameters are listed in Table 2, and the corresponding predicted and measured polishing footprint data are shown in Figure 7. On the whole, the predicted results agree well with the measured polishing footprint data, which proves the accuracy of the proposed material removal model. As can be seen from Figure 7, both predicted and measured MRDs increase as the rotational speed rises from 900 rpm to 1300 rpm. This phenomenon can be interpreted from the kinematic perspective. Increasing rotational speed directly raises the relative shear velocity V at each point within the contact zone, increases the interaction frequency between abrasive grains and the workpiece surface per unit time, and thus improves the MRD.

Table 2. Single-factor experimental parameters for rotational speed (solid rubber ball-end tool).

h (mm)	n (rpm)	α (deg)
0.6	900 1100 1300	23

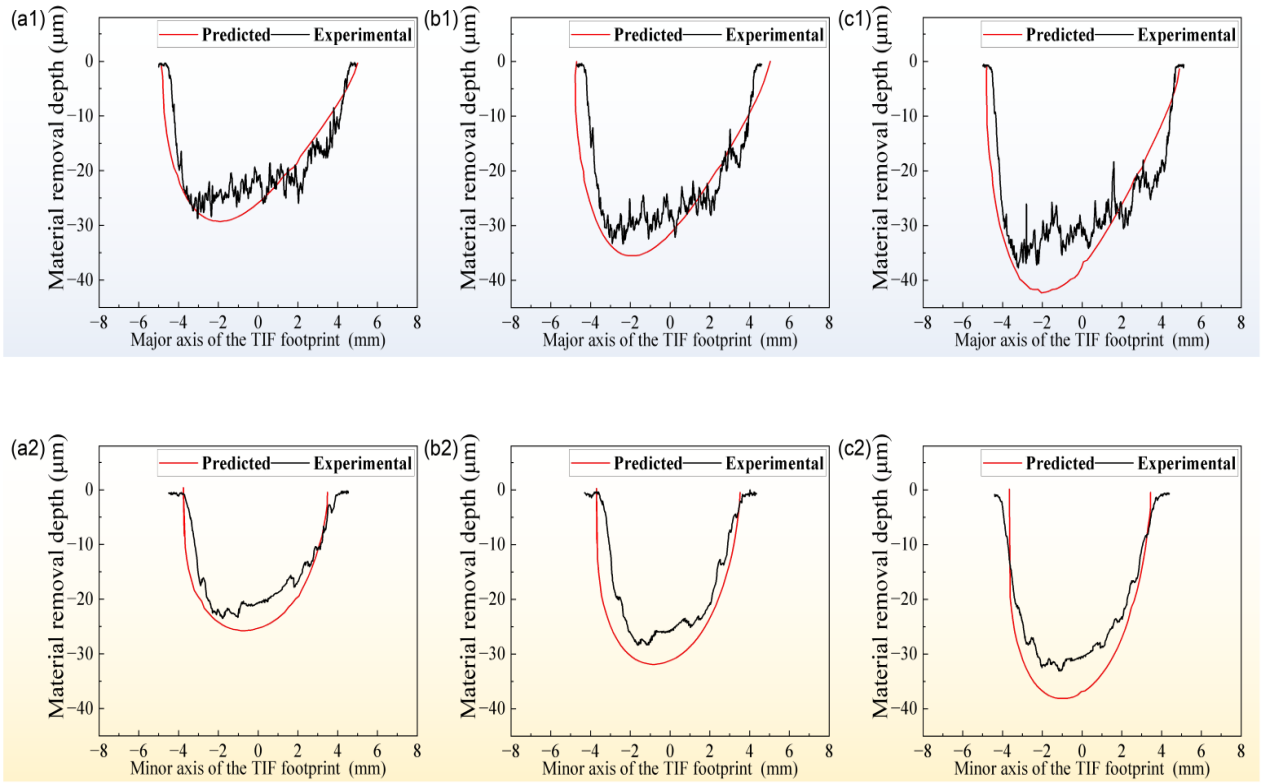


Figure 7. Comparison between predicted and measured polishing footprint data for different rotational speeds. **(a)** n = 900 rpm; **(b)** n =1100 rpm; **(c)** n = 1300 rpm.

3.2.3. Tool offset

Lastly, experiments on tool offset h are performed. Detailed experimental parameters are given in Table 3, and the corresponding predicted and measured polishing footprint results are displayed in Figure 8. Generally, the predicted results match the variation trend of measured polishing footprint

data, showing the reference value of the established material removal model. According to Figure 8, the theoretically predicted MRD increases with increasing tool offset. Incorporated with the data in Figure 6b1,b2 (h = 0.6 mm, n = 1000 rpm, α = 23 deg), the experimental MRD increases when the tool offset grows from 0.6 mm to 0.7 mm. However, as h further increases from 0.7 mm to 0.9 mm, the actual MRD decreases slightly instead. As observed from Figure 8b,c, an inner-concave feature appears at the central region of the practical polishing footprint with h values of 0.8 mm and 0.9 mm.

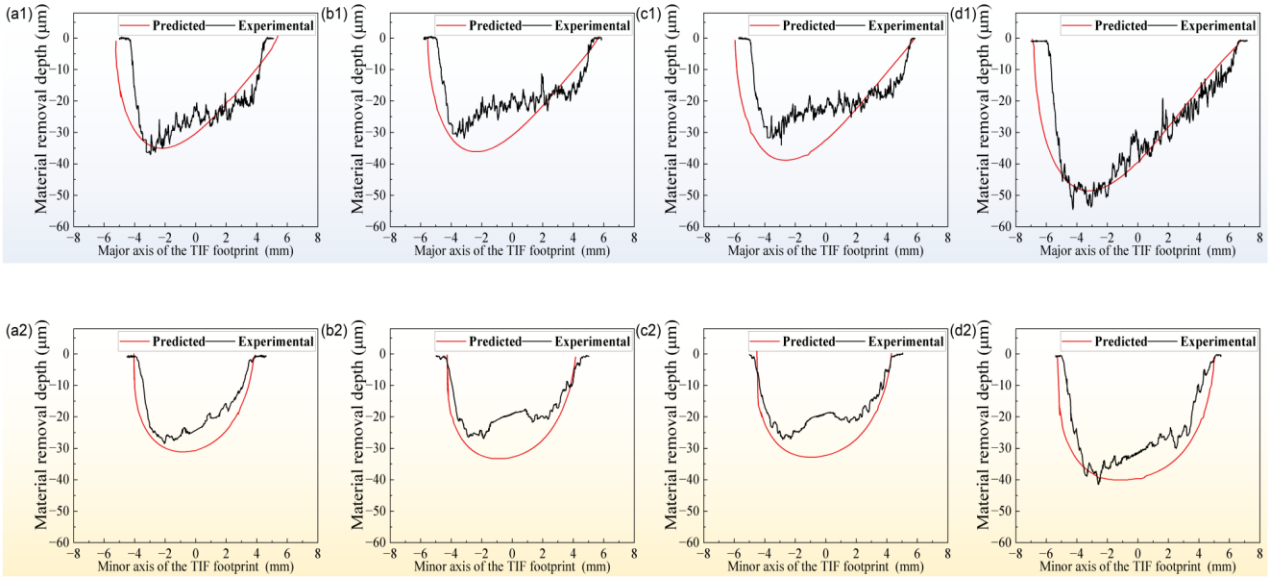


Figure 8. Comparison between predicted and measured polishing footprint data for different tool offsets. **(a)** h = 0.7 mm; **(b)** h = 0.8 mm; **(c)** h = 0.9 mm; **(d)** h = 1.2 mm.

This behaviour can be attributed to the variation of the local contact state with the tool offset. At intermediate tool offsets (0.8 to 0.9 mm), the contact pressure near the centre of the contact zone is relatively high, so the polishing pad is compressed more strongly there and the slurry film in the central contact zone becomes thinner, which in turn modifies the distribution of the abrasive grains. Because the renewal of the slurry in this region is restricted and its replenishment is impeded, the number of abrasive grains that effectively participate in material removal decreases. The removal efficiency in the central region is therefore reduced, and an inner-concave feature is formed.

When the tool offset increases to 1.2 mm, changes in the contact area and pad deformation may modify the local slurry-film distribution and the replenishment of the abrasive grains, potentially alleviating the central removal deficiency. The non-monotonic dependence on the tool offset indicates that the phenomenon is governed jointly by the local contact state, the slurry transport and the effective participation of the abrasive grains rather than by the tool offset alone. Since the model established in this work describes the average macroscopic removal and does not resolve the local slurry-transport conditions inside the contact zone, the inner-concave feature is not reproduced by the predicted profiles.

As can be concluded from Figure 6 to Figure 8, the material removal model established in this work can stably predict the 2D cross-section profiles along the major axis and minor axis for spot polishing with a solid rubber ball-end tool, and can well characterise the asymmetric distortion feature along the minor axis direction.

Table 3. Single-factor experimental parameters for tool offset (solid rubber ball-end tool).

h (mm)	n (rpm)	α (deg)
0.7 0.8 0.9 1.2	1000	23

3.3. Experimental validation with bonnet tool polishing

The material removal model established above has been validated by the preceding experiments using the solid rubber ball-end tool. In order to further investigate the applicability of this model to bonnet polishing, spot polishing experiments are carried out with a bonnet tool in this section. The influences of three key parameters, namely spindle rotational speed, tool offset and inner pressure, on the material removal are examined respectively. By comparing the theoretically predicted 2D profiles along the major axis and minor axis of the polishing footprint with experimental data, the material removal behaviour of bonnet polishing is analyzed, with special attention paid to the prediction capability for the asymmetric distortion feature along the minor axis of the polishing footprint.

3.3.1. Experimental conditions

Spot polishing experiments are performed on a five-axis bonnet polishing machine tool, as depicted in Figure 9. The polishing specimen is fused silica glass with a Young's modulus of 73 GPa and a Poisson's ratio of 0.17. The polishing slurry is prepared by mixing 3 μm-sized cerium oxide powder with deionised water at a mass concentration of 2%, without additional chemical additives. The dwell time for each spot polishing test is 3 s. A 4D interferometer is employed to characterize the polishing footprint morphology.

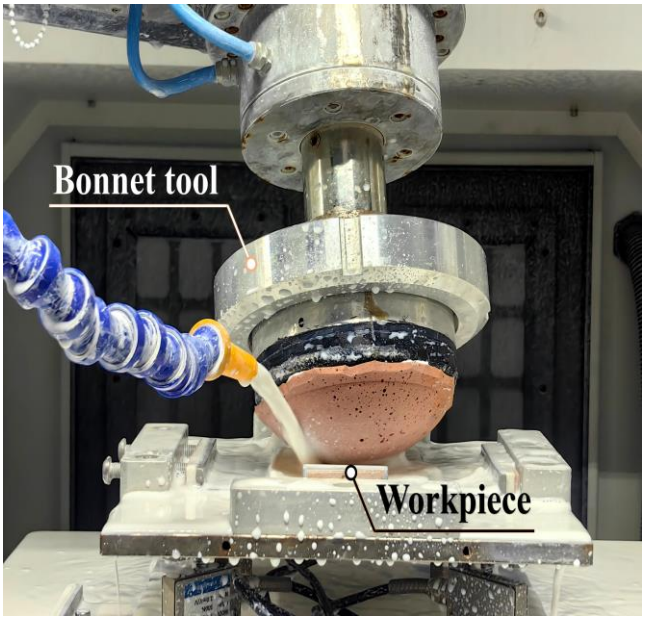


Figure 9. Five-axis bonnet polishing machine tool.

It should be noted that k_1 and k_2 characterize the contributions of the elastic stress component and the dissipative stress component to material removal, respectively, and their values depend on specific processing conditions. For the bonnet tool, variation in inner pressure changes the equivalent stiffness

of the tool as well as the interfacial contact state. Accordingly, k_1 and k_2 must be redetermined when the inner pressure is altered. Furthermore, the change in spindle rotational speed not only modifies the shear velocity within the contact zone but may also alter the actual friction, lubrication and abrasive action states at the polishing interface. Previous studies [16] have demonstrated that spindle rotational speed affects the value of the Preston coefficient. In this work, the two Preston coefficients are determined according to the inner pressure, hence, the same pair of k_1 and k_2 is adopted as long as the inner pressure remains unchanged. Nevertheless, spindle rotational speed also exerts an influence on the coefficients. Therefore, under certain processing conditions, k_1 and k_2 should be re-evaluated when the rotational speed varies even if the inner pressure stays constant. For rotational speed cases where obvious deviations exist between theoretical predictions and experimental results, k_1 and k_2 need to be recalculated to reflect the influence of variation in the actual machining state on material removal behaviour.

3.3.2. Spindle rotational speed

Single-factor experiments regarding rotational speed are first conducted. Detailed experimental parameters are summarised in Table 4, and the corresponding predicted and measured polishing footprint data are presented in Figure 10. As shown in Figure 10, with the rotational speed increasing from 500 rpm to 1333 rpm, both the predicted and measured MRDs for the 2D profiles along the major axis and minor axis of the polishing footprint generally exhibit an increasing trend. This variation tendency is basically consistent with that observed in the foregoing solid rubber ball-end tool polishing experiments.

Under an inner pressure $P_{inner} = 0.1$ MPa listed in Table 4, the same set of Preston coefficients, $k_1 = 3.32611 \times 10^{-13}$ and $k_2 = 2.80405 \times 10^{-12}$, is in principle adopted for all rotational speed cases. It should be noted that, among the six rotational speed conditions shown in Figure 10, this fixed set of coefficients yields satisfactory predictions of the measured material removal profiles along both the major and minor axes for five conditions (500, 667, 1000, 1167 and 1333 rpm), whereas a prominent deviation occurs only at 833 rpm (Figure 10c). This result indicates that, within a certain range of process parameters, the established model reproduces the trend of the material removal variation induced by the rotational speed change with a fixed pair of k_1 and k_2. It also shows that, although the two coefficients act as equivalent material removal parameters, they are not constants that are completely independent of the machining conditions, and their values may be affected by variations in the actual interfacial contact state. Specifically, a change in rotational speed affects not only the shear velocity in the contact zone but also, potentially, the slurry flow, the action and motion of the abrasive grains, the local lubrication conditions and the dynamic response of the flexible tool, so that the effective removal efficiency can change at a specific speed. For the 833 rpm condition, the coefficients are therefore recalibrated to $k_1 = 2.2847 \times 10^{-13}$ and $k_2 = 1.03739 \times 10^{-12}$, which restores good agreement between the predictions and the measurements. The need for recalibration is thus confined to one condition of the series, and all six profiles are well reproduced by the same model expression. This indicates that the model form is able to describe the process and that the limitation lies in the fixed-coefficient assumption rather than in the structure of the model. Overall, these results indicate that the proposed material removal model remains applicable to characterizing the evolution of the polishing footprint profiles along both the major and minor axes across different rotational speeds in bonnet polishing.

Table 4. Single-factor experimental parameters for rotational speed (bonnet tool).

h (mm)	n (rpm)	α (deg)	Inner pressure P_{inner} (MPa)
0.4	500 667 833 1000 1167 1333	23	0.1

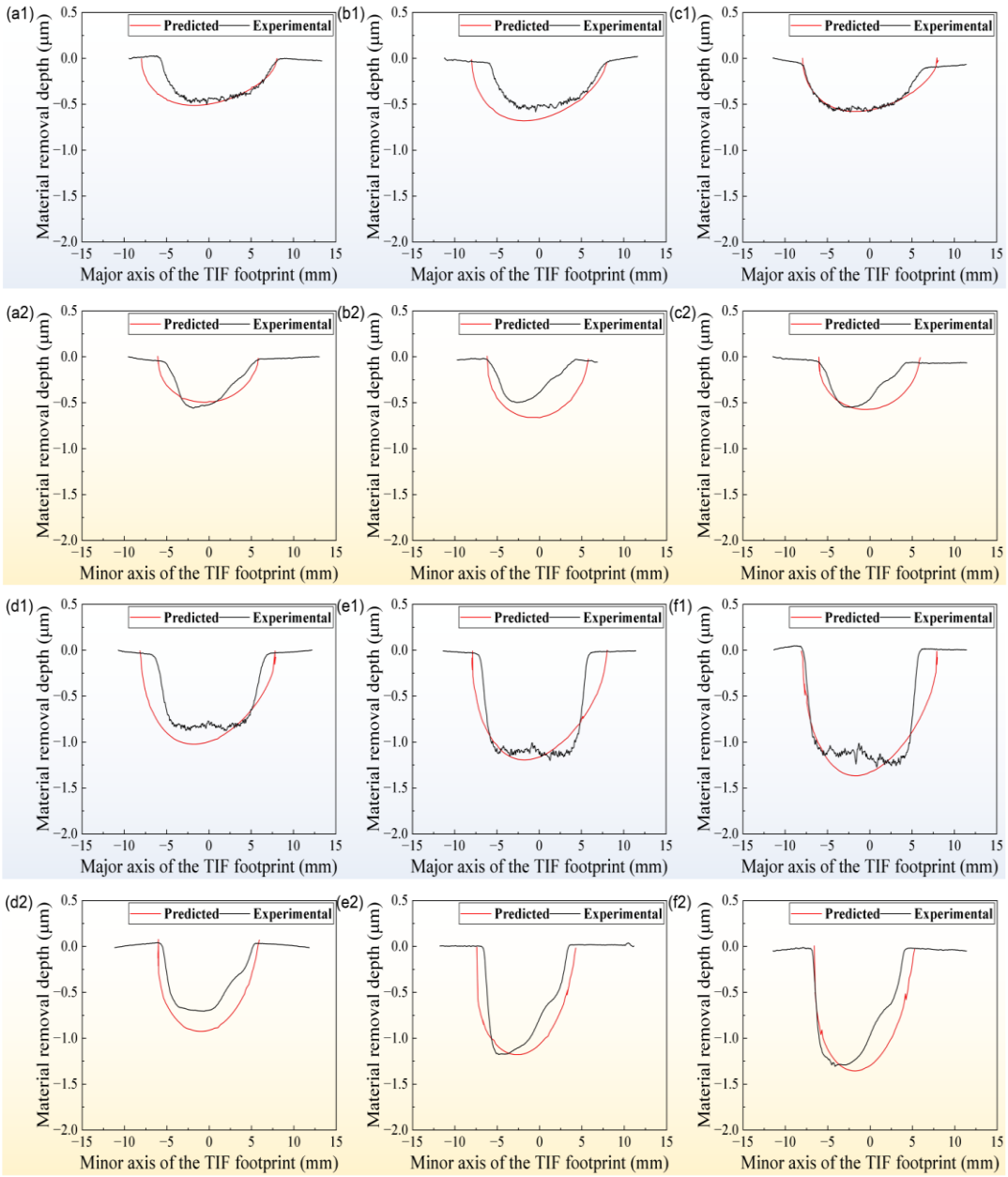


Figure 10. Comparison between predicted and measured polishing footprint data under different rotational speeds. **(a)** n = 500 rpm; **(b)** n = 667 rpm; **(c)** n = 833 rpm; **(d)** n = 1000 rpm; **(e)** n = 1167 rpm; **(f)** n = 1333 rpm.

3.3.3. Tool offset

Next, experimental investigations on tool offset are implemented. Detailed experimental parameters are given in Table 5, and the corresponding predicted and measured polishing footprint results are shown in Figure 11. Overall, both theoretical and experimental MRDs increase with the growth of tool offset. With the spindle rotational speed fixed at 1333 rpm and the inner pressure kept at 0.1 MPa as listed in Table 5, the same pair of Preston coefficients $k_1 = 3.32611 \times 10^{-13}$ and $k_2 = 2.80405 \times 10^{-12}$ is used for all tool offset cases. As can be seen from Figure 11, the developed model can well capture the evolution of polishing footprint profiles and material removal along the major axis and minor axis under different tool offsets. Although local deviations still exist between theoretically predicted profiles and experimentally measured curves under some working conditions, the overall profile features are in good consistency. Such prediction deviations may originate from multiple polishing interface interference factors, including abnormal deformation of the bonnet tool in practical polishing processes, slurry transportation, and the abrasive grain participation state in material removal. In general, with given values of k_1 and k_2, the proposed material removal model can satisfactorily describe material removal characteristics under various tool offset conditions. This further verifies its favourable applicability and prediction performance for bonnet tool polishing.

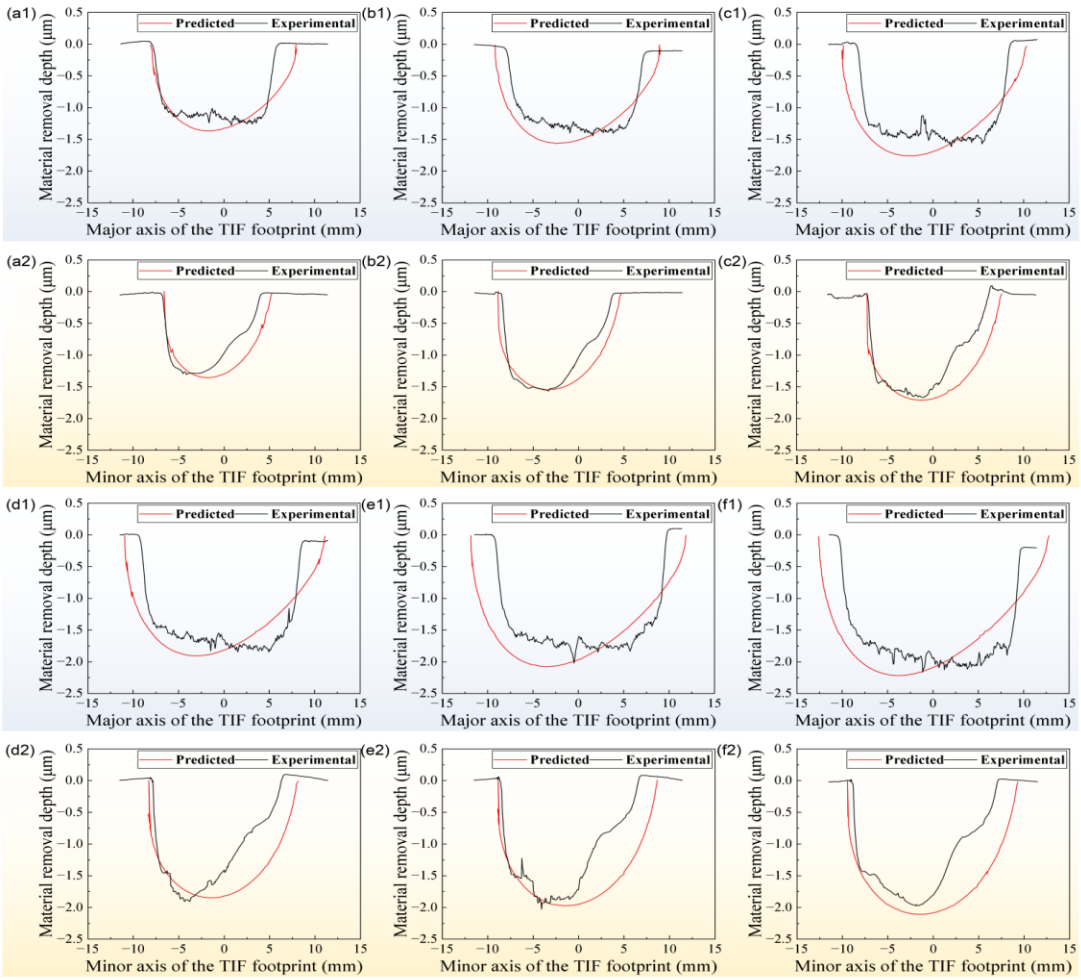


Figure 11. Comparison between predicted and measured polishing footprint data under different tool offsets. **(a)** $h = 0.4$ mm; **(b)** $h = 0.52$ mm; (c) $h = 0.64$ mm; **(d)** $h = 0.76$ mm; **(e)** $h = 0.88$ mm; **(f)** $h = 1.0$ mm.

Table 5. Single-factor experimental parameters for tool offset (bonnet tool).

h (mm)	n (rpm)	α (deg)	Inner pressure P_{inner} (MPa)
0.4 0.52 0.64 0.76 0.88 1.0	1333	23	0.1

3.3.4. Inner pressure

Lastly, experiments focusing on inner pressure P_{inner} are carried out. Detailed experimental parameters are listed in Table 6, and the corresponding predicted and measured polishing footprint results are displayed in Figure 12. Different from spindle rotational speed and tool offset, inner pressure not only affects the contact state between tool and workpiece but also changes the equivalent stiffness of the bonnet tool itself. As illustrated in Figure 12, the experimentally measured MRD increases obviously when the inner pressure rises from 0.1 MPa to 0.15 MPa. Nevertheless, further increasing the inner pressure to 0.2 MPa does not lead to a simple linear growth of MRD. This indicates that material removal does not increase linearly with inner pressure, instead, it is subjected to the coupled effects of bonnet stiffness, interfacial micro-behaviour and pressure distribution characteristics.

Since the variation in inner pressure alters the equivalent stiffness and actual contact state of the bonnet tool, k_1 and k_2 are calibrated separately under different inner pressure levels. For inner pressures of 0.1 MPa, 0.15 MPa and 0.2 MPa, the corresponding Preston coefficients are $k_1 = 3.32611 \times 10^{-13}$ and $k_2 = 2.80405 \times 10^{-12}$, $k_1 = 5.6392 \times 10^{-13}$ and $k_2 = 6.60563 \times 10^{-12}$, as well as $k_1 = 5.6392 \times 10^{-13}$ and $k_2 = 2.08159 \times 10^{-12}$, respectively. In terms of profile morphology, the proposed model can well describe the overall profile along the major axis and capture the obvious asymmetric material removal feature along the minor axis under different inner pressure conditions. Despite local discrepancies between theoretical predictions and experimental measurements, the overall polishing footprint morphology and its key variation characteristics with inner pressure can be effectively predicted, which demonstrates the good applicability of the established model for bonnet tool polishing.

Combining the experimental results of solid rubber ball-end tool polishing in Section 3.2 and bonnet tool polishing in Section 3.3, it can be concluded that the material removal model proposed in this paper can satisfactorily characterize the overall polishing footprint profiles under various FBETs and diverse process parameter conditions. Unlike conventional material removal models based on static contact theory, the developed model can well describe the asymmetric material removal distortion feature along the minor axis of the polishing footprint. This study reveals that taking dynamic dissipative effects into consideration helps to elucidate the origin of asymmetric removal features along the minor axis in FBET polishing.

Table 6. Single-factor experimental parameters for inner pressure (bonnet tool).

h (mm)	n (rpm)	α (deg)	Inner pressure P_{inner} (MPa)
0.52	667	23	0.1
			0.15
			0.2

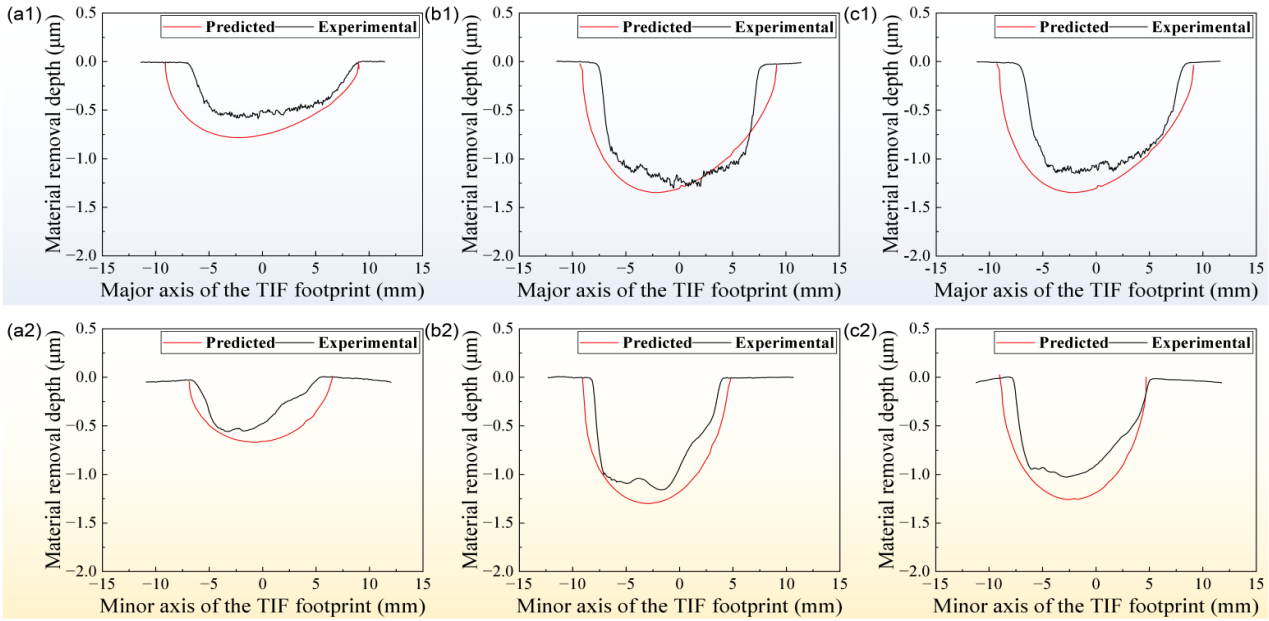


Figure 12. Comparison between predicted and measured polishing footprint data under different inner pressures. **(a)** P_{inner} = 0.1 MPa; **(b)** P_{inner} = 0.15 MPa; **(c)** P_{inner} = 0.2 MPa.

3.4. Further discussion

This section further evaluates the proposed model, focusing on the applicability of the stress-decomposition approach, its quantitative predictive accuracy, and its applicability to the two flexible ball-end tool (FBET) systems. The differences in the Preston coefficients, the possible sources of prediction deviations, and the scope and limitations of the model are also discussed.

3.4.1. Applicability of the stress-decomposition approach

In Section 2.1, the interfacial contact stress is decomposed into elastic and dissipative components by drawing on the viscoelastic contact framework of Brilliantov and Pöschel [24–26]. Note that the three-phase contact between the abrasive grains, the polishing pad and the workpiece, the lubrication provided by the polishing slurry and the scratching action of the abrasives at the FBET polishing interface differ fundamentally from the rolling friction of a viscoelastic sphere on a rigid plane, so that the classical rolling-friction theory cannot be transferred directly to the polishing interface. This work therefore does not extend the rolling-friction theory of Brilliantov and Pöschel to the polishing interface. What is adopted from that theory is not its dry rolling-friction mechanism but the modelling idea of decomposing the viscoelastic contact stress into elastic and dissipative components, which is used here to describe the asymmetric stress distribution caused by the dynamic contact deformation

during the rotation of the flexible ball-end tool. Although the microscopic processes at the polishing interface are complex, the continuous loading and unloading of the flexible tool during rotation is retained at the macroscopic scale. Because the flexible tool and its polishing pad are viscoelastic, their contact response depends not only on the instantaneous deformation but also on the rate of deformation and on the internal dissipation of the material, so that a rate-dependent dissipative stress component must be considered in addition to the elastic contact stress. This decomposition is therefore used here as a macroscopic description of the contact response of the flexible tool. Moreover, the same modelling idea has a precedent in bonnet polishing, where Cao *et al.* [22,23] proposed a material removal model that takes the dynamic effects into account. Applying the decomposition of the contact stress into elastic and dissipative components to the macroscopic description of the FBET polishing interface is therefore reasonable.

3.4.2. Quantitative evaluation of the prediction accuracy

To further evaluate the prediction performance shown in Sections 3.2 and 3.3 beyond qualitative trend comparisons, quantitative statistical metrics are analyzed in this section. The objective of this work is to predict the macroscopic material removal profile of the TIF and its asymmetric distortion along the minor axis during flexible ball-end tool polishing, rather than the microscopic surface roughness or the local topography produced by the random action of individual abrasive grains. The measured two-dimensional profile curves contain high-frequency fluctuations caused by surface roughness, the random action of abrasive grains and measurement noise, whereas the model established in this work is based on continuum contact mechanics and macroscopic material removal theory and therefore inherently describes a smooth macroscopic removal trend. If the global RMSE or R^2 were calculated directly from the raw measured profiles, the result would contain both the macroscopic profile prediction error and the microscopic surface fluctuation, which would amplify the error of the model at a scale that is not the scale of interest and would therefore not reflect the capability of the model to predict the macroscopic TIF morphology.

For the above reasons, the mean relative error of the maximum material removal depth is adopted as the primary quantitative metric. As shown in Figures 13 and 14, for the solid rubber ball-end tool the smallest relative error of the maximum material removal depth is 1.7% and the largest occurs under the working condition with a precession angle of 25 degree. The mean relative errors along the major and minor axes are 11.4% and 16.9%, respectively. For the bonnet tool the smallest relative error is 0.5% and the largest occurs under the working condition with the lowest inner pressure of 0.1 MPa. The mean relative errors along the major and minor axes are 9.6% and 10.9%, respectively. For a few working conditions the relative error of the removal depth is relatively large, because the polishing process involves complex interfacial conditions, such as the actual contact pressure distribution, the slurry supply, the embedding and motion of the abrasive grains and the local friction state, which a macroscopic continuum model cannot fully reproduce. In terms of the mean relative errors, however, the prediction error of the model is of the order of 10% for both tools, which indicates that the proposed model is still able to quantitatively predict the maximum material removal depth of the two types of flexible ball-end tools under the working conditions investigated.

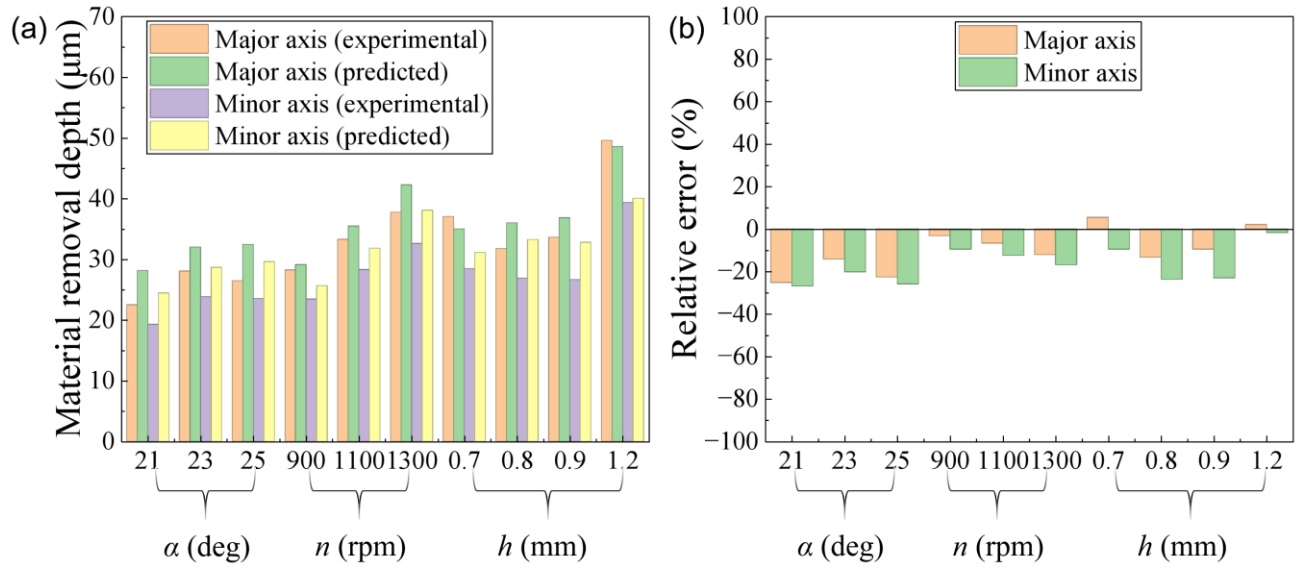


Figure 13. Maximum material removal depth of the solid rubber ball-end tool obtained by prediction and by measurement over the ten working conditions examined. **(a)** Comparison between the predicted and the measured maximum material removal depth; **(b)** Relative error.

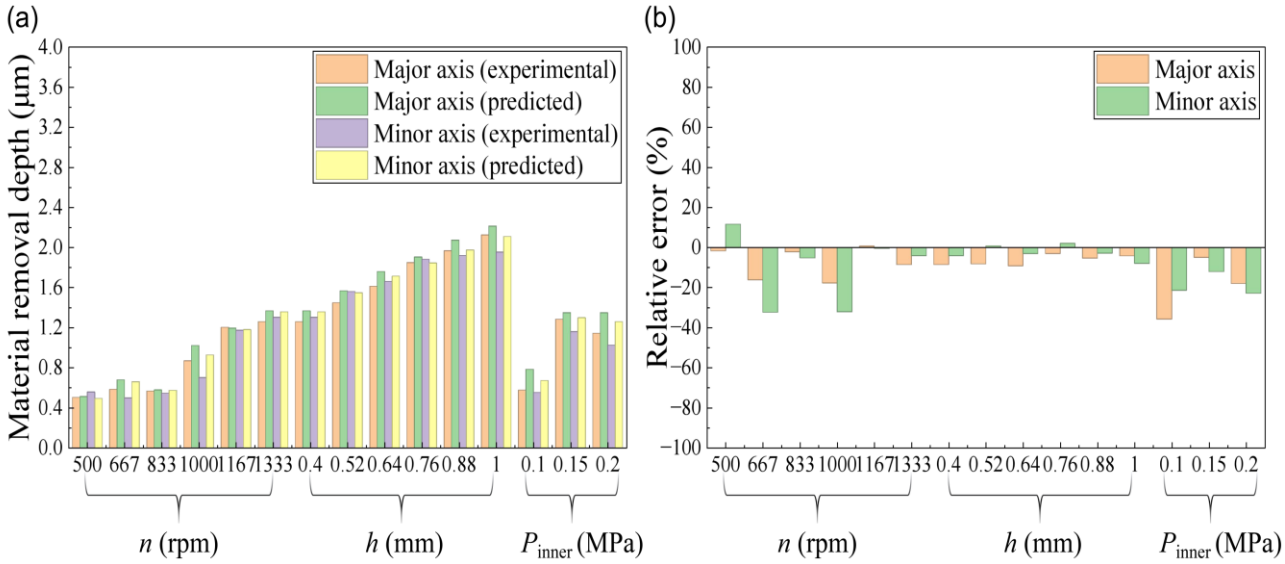


Figure 14. Maximum material removal depth of the bonnet tool obtained by prediction and by measurement over the fifteen working conditions examined; **(a)** Comparison between the predicted and the measured maximum material removal depth; **(b)** Relative error.

3.4.3. Unified description of the two flexible ball-end tools

As demonstrated in Sections 3.2 and 3.3, the proposed model successfully predicts the TIF profiles for both the solid rubber ball-end tool and the bonnet tool, even though the two tools differ appreciably in structure, deformation and contact response. Specifically, the model established in this work does not explicitly introduce additional geometric parameters for the different tool structures. Instead, the equivalent elastic modulus E^* and the Preston coefficients are used to describe the differences between the flexible tools under actual machining conditions. For the solid rubber ball-end tool, the equivalent elastic modulus E^* is a constant determined by the properties of the rubber material, and the contact area

and the pressure distribution can be calculated directly from this fixed modulus on the basis of the Hertzian contact assumption. For the bonnet tool, the inner pressure not only affects the contact state between the tool and the workpiece but also changes the equivalent stiffness of the tool itself. The variation of the Preston coefficients provides direct evidence of how this modification acts on the contact mechanics. A higher inner pressure tensions the bonnet, which increases the equivalent stiffness and enlarges the contact area, so that a larger fraction of the applied load is transmitted through the elastic contact. When the bonnet is highly tensioned, however, the energy dissipated in its loading-unloading cycle is reduced, so that the material removal no longer grows linearly with the inner pressure, in agreement with the observed dependence of the Preston coefficients on the inner pressure in Section 3.3.4. Over the investigated range, the inner pressure therefore influences the contact mechanics through the equivalent stiffness of the tool, and its effect on material removal is captured quantitatively by the Preston coefficients. A fully explicit constitutive relation between the inner pressure and the equivalent elastic modulus would require a mechanical model of the bonnet and is left for future work. In summary, a unified material removal model is applied to the different flexible tools, in which the tool structure is represented by the equivalent elastic modulus E^*, while the influence of the machining conditions is captured by the corresponding Preston coefficients.

3.4.4. Comparison of the Preston coefficients for the two flexible tool systems

A comparison of the k_1 and k_2 values obtained for the two experimental systems reveals noticeable differences, which are accounted for by three main factors. (1) The workpiece materials are different: the solid rubber ball-end tool is used on S136 steel and the bonnet tool on fused silica, and the two materials differ in elastic properties, surface structure and material removal behaviour under the action of the abrasive grains, so that both the elastic and the dissipative contributions to removal differ. (2) The tools are different: the solid rubber ball-end tool is made of solid rubber, whereas the bonnet tool consists of a polyurethane polishing pad bonded to an elastic ball-end substrate, so that the two have different equivalent elastic moduli and therefore differ in their deformation and dissipation response during dynamic contact. (3) The abrasive type and the removal mechanism are different: the slurry used for S136 steel is an alumina slurry with an average particle size of 4 μm at a mass concentration of 5%, whereas fused silica is polished with a cerium oxide slurry with an average particle size of 3 μm at a mass concentration of 2%, and the two abrasives operate through different chemical-mechanical removal routes. In addition, the two experimental systems differ in measuring instrument, dwell time (2 minutes *versus* 3 seconds) and the process window explored, so that the absolute values of k_1 and k_2 should be compared qualitatively rather than as a direct measure of removal efficiency.

3.4.5. Attribution of the prediction deviations

Although the overall profile evolution is well captured in Figures 6 to 12, local deviations still exist between the predicted curves and the experimental measurements under certain working conditions. These deviations stem from either theoretical model assumptions or experimental factors. From the point of view of the theoretical model, the present work mainly uses the static Hertzian contact theory to describe the static contact stress and introduces a dissipative stress component to describe the dynamic contact stress. The model reflects the influence of the macroscopic contact stress and of the relative shear

velocity on material removal, but it is still based on a number of simplifying assumptions. For example, it does not explicitly consider the local flow of the polishing slurry or the spatial distribution of the abrasive grains, nor does it fully describe a possible nonlinear viscoelastic response or the complex contact deformation of the flexible tool. Under some working conditions the actual contact pressure and removal efficiency may therefore deviate from those assumed in the theoretical model.

From the experimental point of view, the actual polishing process may be affected by the random action of the abrasive grains, fluctuations of the slurry supply, changes in the tool and pad condition, machining errors and measurement noise, all of which may cause local irregular fluctuations in the measured profiles. These fluctuations are not reproduced by the model, which describes the macroscopic removal of a continuum and therefore yields a smooth profile. On this basis, the deviations are attributed case by case as follows. The largest deviations originate from the assumptions of the model: at the lowest inner pressure the actual contact pressure departs most from the idealised Hertzian contact, and at a precession angle of 25 degree the reduction in the effective number of abrasive grains caused by the shortened ploughing trajectory is not represented by the model. The deviation at 833 rpm may result from a combination of experimental and theoretical factors, so that the Preston coefficients have to be recalibrated for this condition. The localized deviations at tool offsets of 0.8 and 0.9 mm are consistent with the slurry-renewal effect discussed in Section 3.2.3, which lies outside the scope of the present model. Apart from the cases discussed above, the measured and the predicted profiles follow the same trend, and the residual local irregularities are dominated by experimental factors.

3.4.6. Applicability boundary of the model

Regarding the local irregular fluctuations noted above, it should be emphasized that the material removal model established in this work is a macro-scaled TIF model. Its solution variable is the material removal depth, its purpose is to predict the two-dimensional morphology of the polishing footprint and to support the surface form convergence in deterministic polishing, and it describes material removal in an average sense only. It does not consider the microscopic scratching of a single abrasive grain, the microscopic plastic removal of the material or local random disturbances of the slurry, which is why its output is a smooth profile. The high-frequency irregular fluctuations observed in the experimental curves originate from the random cutting of abrasive grains, the surface texture of the polishing pad and the non-uniform distribution of the abrasive grains, and they reflect the surface roughness characteristics of the workpiece after polishing. The present model is not capable of predicting the surface roughness directly. To predict the surface roughness, a micro-scaled material removal model would have to be introduced that takes into account the abrasive size, the number density of the abrasive grains, the depth of cut of a single abrasive grain and the surface topography of the polishing pad. It should also be noted that the high-frequency fluctuations of the experimental curves are not equivalent to surface roughness, and that a rigorous roughness analysis would require a specified measurement resolution, a defined filter cut-off wavelength and an appropriate surface topography evaluation standard. Accordingly, the proposed model is mainly used to predict the macroscopic two-dimensional profile of the elliptical polishing footprint, in particular the asymmetric material removal feature along the minor axis, and it provides the basis for determining the dwell time in deterministic polishing. The prediction of surface roughness requires the coupling of an independent micro-scaled material removal model, which is the focus of the next stage of our work.

4. Conclusions

Aiming at two typical FBET polishing technologies, namely bonnet polishing and solid elastic ball-end tool polishing, this work investigates the asymmetric material removal distortion feature along the minor axis of the polishing footprint. A material removal model considering dynamic dissipative effects is established and validated by spot polishing experiments. The main findings and conclusions are summarised as follows:

(1) During FBET polishing, the tool undergoes continuous rotational entry-exit motion along the minor axis of the polishing footprint. Accordingly, the contact interface between tool and workpiece exhibits prominent dynamic characteristics. Conventional material removal models based on the static Hertz contact theory cannot adequately explain the material removal asymmetry along the minor axis of the polishing footprint. By introducing the dissipative stress component, the proposed material removal model can quantitatively describe the shift in pressure distribution induced by dynamic contact, and further reveal the formation mechanism of asymmetric material removal distortion along the minor axis of the polishing footprint.

(2) The static elastic stress component and dynamic dissipative stress component are incorporated into the classical Preston model. Two Preston coefficients k_1 and k_2 are introduced to characterize the distinct contributions of these two stress components to material removal. Experimental results demonstrate that the developed material removal model can satisfactorily predict the 2D profiles along both the major axis and minor axis of the polishing footprint as well as their evolution with varying process parameters. Moreover, this model is applicable to both typical FBET polishing processes, *i.e.*, bonnet polishing and solid elastic ball-end polishing.

Data availability statement

No supplementary or additional data were generated in this study.

Declaration of generative AI and AI-assisted technologies

The authors did not use generative AI or AI-assisted technologies in the writing of this manuscript.

Acknowledgments

This work was financially supported by the Special Program for Stable-Support Funding of SASTIND. We sincerely appreciate the invaluable feedback and suggestions provided by all anonymous reviewers. Furthermore, we express our deep gratitude to those who have offered their quiet support and assistance throughout this process.

Authors' contribution

Conceptualization, P.L. ; methodology, P.L.; software, J.W.; validation, B.Z.; formal analysis, Q.W.; investigation, P.L; resources, C.S.; data curation, P.L; writing—original draft preparation, P.L; writing—review and editing, Z.H.; visualization, L.Z.; supervision, B.G.; project administration, C.S.; funding acquisition, C.S. All authors have read and agreed to the published version of the manuscript.

Conflicts of interest

The authors declare no conflicts of interest.

References

[1] Wang S, Liu Y, Niu Z, Yu J, Kong M, *et al.* Automated real-time evaluation system for laser-induced damage of optical components based on microscopic scattering dark-field imaging method. *Phys. Lett. A*. 2025, 546:130530.

[2] Guo S, Wang S, Wang S, Wu L, Liu D. Dark-field surface defects detection method for multi-surface-shape large aperture optical components. *Appl. Opt.* 2024, 63(25):6686–6695.

[3] McElwain MW, Feinberg LD, Perrin MD, Clampin M, Mountain CM, *et al.* The James Webb Space Telescope Mission: optical telescope element design, development, and performance. *Publ. Astron. Soc. Pac.* 2023, 135(1047):058001.

[4] Zhang X, Hai K, Li Z, Zhang Y, Zhang B, *et al.* Present situation, problems and suggestions of advanced optical ultra-precision manufacturing technology. *Bull. Chin. Acad. Sci.* 2025, 40(5):870–878.

[5] Duy TN, Quang NM, Van Que N. Surface quality and material removal via viscosity-controlled Magnetorheological finishing Ti-6Al-4V using Fe_3O_4-SiO_2 abrasives and Halbach array. *Results Eng.* 2025, 26:105089.

[6] Wang Y, Wu X, Kang R, Guo X, Gao S. Theoretical and experimental investigation on material removal modeling in active fluid jet polishing of optical components. *J. Manuf. Processes.* 2025, 155:156–170.

[7] Tang X, Song Z, Xie K, He R, Jin M. Contact pressure prediction model for structurally-optimized small elastic polishing tool on curved optical components. *Int. J. Adv. Manuf. Technol.* 2026, 144:6693–6710.

[8] Wang X, Shao X, Zhou K, Guo L, Wang J, *et al.* Study on the effect of dispersed phase particle functional groups on the polishing performance of shear-thickening polishing slurry. *Precis. Eng.* 2025, 94:291–302.

[9] Qu S, Sun X, Dong Z, Mu S, Zhao H, *et al.* The effect of novel silica-based polishing solution on the UV-CMP performances of K9 optical glass. *Ceram. Int.* 2026, 52(2):2043–2059.

[10] Qu S, Cui Z, Chu X, Sun X, Dong Z, *et al.* Study on the polishing mechanism under the combined effect of K_2CO_3, KH550 and ultrasonic vibration for K9 optical glass. *Appl. Surf. Sci.* 2025, 693:162746.

[11] Lin Z, Li X, Chen G, Zhang P, Cao Y, *et al.* A review of material surface processing utilizing gas cluster ion beam technology. *Eur. Phys. J. D.* 2025, 79(5):50.

[12] Zhang P, Wang Z, Huang X, Zhang H. Application and development of bonnet polishing technology. *Opt. Eng.* 2024, 63(10):100901.

[13] Rao M, Zhang F, Zhang Y, Wei C, Yin Y. Multiscale modeling of tool influence function in bonnet polishing using pad surface topography histogram. *Tribol. Int.* 2026, 215:111466.

[14] Zang Y, She Z, Liu C, Ke J, Chu J, *et al.* Modeling and analysis of elastic mechanics-based tool influence function for robotic polishing of single-crystal silicon. *Precis. Eng.* 2026, 102:75–90.

[15] Cheung C, Kong L, Ho L, To S. Modelling and simulation of structure surface generation using computer controlled ultra-precision polishing. *Precis. Eng.* 2011, 35(4):574–590.

[16] Pan R, Zhong B, Chen D, Wang Z, Fan J, *et al.* Modification of tool influence function of bonnet polishing based on interfacial friction coefficient. *Int. J. Mach. Tools Manuf.* 2018, 124:43–52.
[17] Wang C, Wang Z, Yang X, Sun Z, Peng Y, *et al.* Modeling of the static tool influence function of bonnet polishing based on FEA. *Int. J. Adv. Manuf. Technol.* 2014, 74(1–4):341–349.
[18] Deng Y, Guo X, Kang R, Gao S. Multi-factor and multi-scale material removal function modeling and experimental validation for bonnet polishing of freeform optical elements. *Tribol. Int.* 2025, 210:110757.
[19] Shi C, Peng Y, Hou L, Wang Z, Guo Y. Micro-analysis model for material removal mechanisms of bonnet polishing. *Appl. Opt.* 2018, 57(11):2861–2872.
[20] Fatahian H, Mishra R, Fleming L, Fatahian E, Akar Y, *et al.* Hybrid CFD–machine learning framework for predicting material removal rates in bonnet polishing. *Precis. Eng.* 2026, 100:481–498.
[21] Shi C, Wang C, Cheung CF, Zhang Z, Li Z, *et al.* Curvature effect-based modeling and experimentation of the material removal in polishing optical surfaces using a flexible ball-end tool. *Opt. Express*. 2022, 30(14):24611–24638.
[22] Cao Z, Cheung CF, Zhao X. A theoretical and experimental investigation of material removal characteristics and surface generation in bonnet polishing. *Wear* 2016, 360–361:137–146.
[23] Cao Z, Cheung CF. Multi-scale modeling and simulation of material removal characteristics in computer-controlled bonnet polishing. *Int. J. Mech. Sci.* 2016, 106:147–156.
[24] Brilliantov NV, Pöschel T. Rolling friction of a viscous sphere on a hard plane. *Europhys. Lett.* 1998, 42(5):511–516.
[25] Shixiong X, Yun Z, Yonghong D, Yue H, Zhongjun C. Prediction of the material removal rate in bonnet polishing using a Bayesian optimization deep neural network. *Opt. Express*. 2024, 32(24):42810–42825.
[26] Barber JR. *Contact Mechanics*. Cham: Springer International Publishing, 2018. pp. 2705–2708.
[27] Qu S, Wang Z, Zhang C, Ma Z, Zhang T, *et al.* Material removal profile prediction and experimental validation for obliquely axial ultrasonic vibration-assisted polishing of K9 optical glass. *Ceram. Int.* 2021, 47(23):33106–33119.
[28] Pan R, Zhao W, Zhong B, Chen D, Wang Z, *et al.* Evaluation of removal characteristics of bonnet polishing tool using polishing forces collected online. *J. Manuf. Process*. 2019, 47:393–401.
[29] Zheng QJ, Zhu HP, Yu A. Finite element analysis of the rolling friction of a viscous particle on a rigid plane. *Powder Technol.* 2011, 207(1–3):401–406.
[30] He Z, Hai K, Li K, Yu J, Wu L, *et al.* Research on the influence of the material removal profile of a spherical polishing tool on the mid-spatial frequency errors of optical surfaces. *Micromachines* 2024, 15(5):654.
[31] Zhao Z, Xiong J, Li L, Wang H, Lin J, *et al.* Fundamental study of surface generation in robot-assisted polishing of optical components. *Int. J. Adv. Manuf. Technol.* 2025, 137(5):2221–2235.
[32] Chen HC, Lin JT, Lo YH, Liu CW. Material removal and tool path ripple error of bonnet polishing using pads with different groove patterns. *Int. J. Adv. Manuf. Technol.* 2024, 132(11):5895–5905.
[33] Shi C, Huang Z, Zhang X, Chen Z, Wang G, *et al.* Experimental investigation of tribological behavior of textured pads and their potential application in flexible ball-end tool polishing. *J. Clean. Prod.* 2025, 524:146527.

[34] Huang X, Wang Z, Li L, Luo Q. Research on the modification of the tool influence function for robotic bonnet polishing with stiffness modeling. *Rob. Comput. Integr. Manuf*. 2024, 86:102674.

[35] Kang N, Yin S, Li R, Zhou R, Guo X. Evolution of hybrid material removal under workpiece rotation in ultra-precision small tool polishing. *Tribol. Int.* 2027, 226:112740.

[36] Pan R, Chen C, Yuan Z, Li Y, Chen D, *et al.* Optimization of optical component shaping and polishing process based on iterative correction of material removal function. *Int. J. Precis. Eng. Manuf.* 2026, 27(7):2805–2823.